

# Large-amplitude behavior of the Grinfeld instability: a variational approach

Peter Kohlert<sup>1</sup>, Klaus Kassner<sup>1</sup>, and Chaouqi Misbah<sup>2</sup>

<sup>1</sup> Institut für Theoretische Physik, Otto-von-Guericke-Universität Magdeburg, Postfach 4120, D-39016 Magdeburg, Germany

<sup>2</sup> Groupe de Recherche sur les Phénomènes hors de l'Équilibre, LSP, Université Joseph Fourier (CNRS), Grenoble I, B.P. 87, Saint-Martin d'Hères, 38402 Cedex, France

Received: date / Revised version: date

**Abstract.** In previous work, we have performed amplitude expansions of the continuum equations for the Grinfeld instability and carried them to high orders. Nevertheless, the approach turned out to be restricted to relatively small amplitudes. In this article, we use a variational approach in terms of multi-cycloid curves instead. Besides its higher precision at given order, the method has the advantages of giving a transparent physical meaning to the appearance of cusp singularities and of not being restricted to interfaces representable as single-valued functions. Using a single cycloid as ansatz function, the entire calculation can be performed analytically, which gives a good qualitative overview of the system. Taking into account several but few cycloid modes, we obtain remarkably good quantitative agreement with previous numerical calculations. With a few more modes taken into consideration, we improve on the accuracy of those calculations. Our approach extends them to situations involving gravity effects. Results on the shape of steady-state solutions are presented at both large stresses and amplitudes. In addition, their stability is investigated.

**PACS.** 47.20.Hw Morphological instability; phase changes – 05.70.Ln Nonequilibrium and irreversible thermodynamics – 46.25.-y Static elasticity – 81.10.Aj Theory and models of crystal growth; physics of crystal growth, crystal morphology and orientation

## 1 Introduction

When a nonhydrostatically strained solid has a surface, at which material can be redistributed by some appropriate transport mechanism, it may reduce its elastic energy via surface undulations. Intuitively, this should be clear: stresses are partially relieved in the maxima of corrugations and enhanced in their minima. The elastic energy density is therefore reduced in the maxima and increased in the minima, favoring growth of the former and deepening of the latter. This mechanism is at the origin of a morphological instability leading to the formation of grooves with a relatively well-defined initial spacing under uniaxial stress [1, 2] and, possibly, the evolution of islands, if the stress is biaxial [3, 4]. Pertinent transport processes are melting-crystallization for a solid in contact with its melt and surface diffusion for a sufficiently hot solid in vacuum. The latter case is relevant in epitaxial growth, where the lattice mismatch between different materials is the source of biaxial stress.

The instability seems to first have been predicted by Asaro and Tiller [5], but its universal nature was recog-

nized by Grinfeld [1], hence it has often been referred to as Grinfeld or Asaro-Tiller-Grinfeld (ATG) instability. An unambiguous experimental demonstration of the instability was given by Torii and Balibar [6], using solid helium in contact with its superfluid.

It should be emphasized that the surface undulation evolving as a consequence of the instability is not due to elastic deformation such as bending (as would be the case on application of a pressure to a long thin rod, leading to the Euler buckling instability). Instead, the instability materializes itself via mass transport and is independent of whether the stress is tensile or compressive. When the solid is in contact with its melt, the latter is a particle reservoir, rendering mass transport easy (and the dynamics is not governed by a conservation law). When the solid is in contact with vacuum such as in the case of heteroepitaxy, the instability takes place via surface diffusion in most cases, but may also be supported by other transport processes such as vacancy or impurity diffusion. In that case, mass conservation is important in the dynamics. For a pedagogical introduction into the subject of the ATG instability, we refer the reader to [7].

There are a number of interesting questions concerning the instability. Since it produces crack-like patterns [8], does it constitute a generic route to fracture as hy-

pothesized in [9] or will plasticity in general lead to a restabilization? If one restricts oneself to linear elasticity, are there steady states beyond those found by Spencer and Meiron [10]? It has been shown that in directional solidification stable steady state patterns are realizable [7, 11]. For the pure Grinfeld instability, this appears to be impossible in extended systems. Further questions concern the nature of dynamical states, when there is no steady state. Coarsening has been found to be a generic behaviour [12, 13, 14], but more detailed investigations on large-scale systems would be desirable, to determine the precise form of the pertinent power laws.

Numerical simulations of a solid undergoing the Grinfeld instability [8, 9, 10] have the awkward tendency of producing cusp singularities in finite time. The investigation of Spencer and Meiron [10] has shown that these singularities are not an artifact of the numerics but intrinsic to the continuum model describing the system, under the assumption of linear elasticity (and in the limit of negligible sound propagation effects). What they found was a steady branch of solutions in a certain range of wavelengths, corresponding to very small sinusoidal shapes near the onset of the branch and approaching a cycloid-like cuspy shape near its termination.

Such a result might have been anticipated on the basis of the analytic work by Chiu and Gao [15], who performed a detailed calculation of the stress state under a cycloid-shaped surface using the Goursat function scheme proposed by Mußchelischwili [16]. All of these numerical studies considered two-dimensional systems where the interface is described by a curve. Whereas we have treated three-dimensional systems in [4] within a weakly nonlinear approach, we will restrict ourselves to two dimensions here but go well beyond the regime of validity of weakly nonlinear theory.

Chiu and Gao find that for a certain range of wavenumbers a fully cusped cycloid constitutes an energetically more stable configuration than a flat surface. In section 2, we will show that a variational calculation using cycloids as ansatz functions gives a rather good approximation of steady state solutions of arbitrary amplitude, some of which were discussed in [10].

Moreover, we are able to draw conclusions on the large amplitude behavior even for strong gravity or a large density difference between the solid and nonsolid phases (liquid or vacuum), as we show in section 3. Evidence for these states has already been found in [17].

In section 4, we present a generalization of this idea. Employing a special system of (not necessarily univalent) functions called multi-cycloids we analytically recover the numerical results for the mean square amplitude to excellent accuracy already at third order. At higher order, we get more precise results with less numerical effort than Ref. [10].

Finally, we give some conclusions as to the physical interpretation of our results and suggest how to verify them experimentally or by a full numerical computation.

## 2 The mono-cycloid approximation

### 2.1 Cycloids

We wish to use cycloids and more general curves deriving from cycloids to model the steady-state surface pattern of a two-dimensional solid after it has undergone the Grinfeld instability. This is of course motivated by the fact that cycloids have been shown by Chiu and Gao [15] to be very efficient in reducing the elastic energy, and hence the final steady state, if any, should be close to a cycloid shape.

Cycloids belong to the more generic class of trochoids, curves defined as the trace of a point fixed on a circle rolling along some prescribed line. A cycloid is the curve traced out by a point on the circumference of a circle as the latter rolls along a straight line. When we put the point inside or outside the circle instead, we obtain a curtate or a prolate cycloid, respectively. The parametric representation of a cycloid can be given in a compact manner by a complex generating function

$$\zeta(\xi) = \xi - i \frac{\rho}{k} e^{-ik\xi}, \quad (1)$$

Herein,  $i$  is the imaginary unit,  $k$  is a wavenumber and  $\rho$  is a dimensionless amplitude-like parameter. The cycloid is obtained by taking the real and imaginary part as the  $x$  and  $y$  coordinates, respectively.

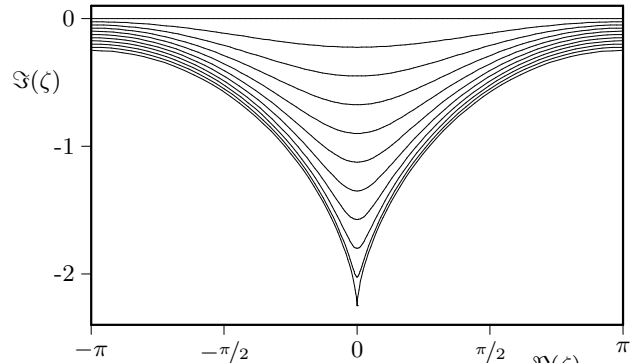


**Fig. 1.** Cycloids, as in equation (1) with  $k = 1$ , plotted in the range  $\xi = (-\pi, \pi)$ ;  $\rho = 0 \dots 1$  from top to bottom. Curves have been shifted in order to avoid overlapping.

Taking  $\rho = 1$  leads to the representation of the classical, i.e., cusped, cycloid. Choice of a plus instead of the minus sign in equation (1) would just shift the minimum from  $\xi = 0$  to  $\xi = \pi/k$ , while a plus sign in the exponent would lead to a surface with the cusps pointing upward. The latter case is of no relevance for the Grinfeld instability, because a fully relaxed upward cusp would immediately shrink under any perturbation in order to decrease the surface energy.

For  $\rho > 1$ , the cycloid becomes self-intersecting and does not represent a physical state anymore. Note, however, that if we “superimpose” several cycloids<sup>1</sup> as we will

<sup>1</sup> This is not a superposition in the standard sense. We add up partial representations of the  $x$  and  $y$  coordinates, so the whole curve is not a simple sum, see Eq. (29).

do in section 4, the possibility of the  $x$  coordinate to vary nonmonotonously allows the representation of patterns with overhangs that do not self-intersect. We will not discuss this feature in detail here but report on those patterns in a different article.

The parametric representation of the cycloid is

$$x(\xi) = \Re[\zeta(\xi)] = \xi - \frac{\rho}{k} \sin(k\xi), \quad (2a)$$

$$y(\xi) = \Im[\zeta(\xi)] = -\frac{\rho}{k} \cos(k\xi) \quad (2b)$$

Assuming the surface of a solid having undergone the Grinfeld instability to be described by this shape, we shift the cycloid position by its mean value

$$m = \frac{k}{2\pi} \int \dot{x}(\xi)y(\xi) d\xi = \frac{\rho^2}{2k}, \quad (3)$$

in order to keep the average interface position at  $y = 0$ . Herein, the dot denotes differentiation with respect to  $\xi$ . Hence, from now on we use

$$y(\xi) = -\frac{\rho}{k} \cos(k\xi) - \frac{\rho^2}{2k}. \quad (4)$$

Moreover, if we want to compare results with both our amplitude calculation [17] and the work of Spencer and Meiron [10], we additionally have to know the mean square amplitude of the cycloid. As in [17], we denote this mean square amplitude by  $\bar{\alpha}$ ; its calculation yields

$$\bar{\alpha} = \left[ \frac{k}{2\pi} \int \dot{x}(\xi)y(\xi)^2 d\xi \right]^{1/2} = \left| \frac{\rho\sqrt{2-\rho^2}}{2k} \right|, \quad (5)$$

where the absolute value ensures a nonnegative mean square amplitude, no matter what the sign of  $\rho$  and of  $k$ .

## 2.2 Scaling

Our basic model is an isotropic solid obeying the laws of linear elasticity (i.e., the Lamé equations) with a surface on which shear stresses vanish while the normal stress component is equal to the negative pressure in the liquid or zero. That is, we neglect capillary overpressure due to a curved interface, which is known to be a small cross effect [7]. Moreover, we neglect the body force effect of gravity in the elastic equations, also known to be small.

The energy of the solid then consists of three contributions, its elastic energy, total surface energy, and potential energy in the gravity field.

It is known [14] that if the latter force, gravity, is completely neglected, the equations of motion of the Grinfeld instability can be made parameter free. This is achieved by referring all lengths to a length scale  $l_1$ , essentially the Griffith length, given by:

$$l_1 = \frac{\gamma}{2w_0}, \quad (6)$$

where  $\gamma$  is the surface tension and  $w_0 = \sigma_0^2(1-\nu^2)/2E$  the elastic energy density of the prestressed planar state.

$\sigma_0 = \sigma_{xx} - \sigma_{zz}$  is the first normal stress difference or, in more physical terms, the excess stress applied in the  $x$  direction, to produce a uniaxially strained solid, whereas  $E$  and  $\nu$  are elastic constants describing an elastically isotropic material, *viz.* Young's modulus and the Poisson number.

Physically, the Griffith length describes the competition between surface energy and elastic energy. It is used predominantly in the theory of crack propagation. Cracks larger than this length relieve more elastic energy when growing than they produce surface energy, while cracks shorter than it can reduce energy only by shrinking. Therefore, this length scale represents a nucleation size for crack generation.

When gravity is considered, another length  $l_2$  becomes important, which is

$$l_2 = \frac{w_0}{g\Delta\rho}. \quad (7)$$

Herein,  $\Delta\rho$  is the density difference between the solid and the second phase,  $g$  the gravitational acceleration. This gravity length describes competition between elastic energy and potential energy in a gravitational field. Due to the density difference between the two phases, the system can gain potential energy, if the phase with the larger density, usually the solid, shifts its center of mass downward. As a consequence, if a solid immersed in and in equilibrium with its melt is submitted to a uniaxial stress, it will first start to melt, because it is now out of equilibrium; but then its center of mass shifts downward, hence the potential energy is decreased and a new equilibrium state may be reached. This happens whenever the applied stress difference is below the instability threshold. The solid surface melts back by a certain height, and this height change is exactly given by  $l_2$ .

The only parameter of the nondimensionalized equations is the ratio of these length scales:

$$l_{12} := \frac{l_1}{2l_2}. \quad (8)$$

In all considerations that follow, we have carried out a formal transformation  $x \rightarrow x/l_1$ ,  $y \rightarrow y/l_1$ ,  $k \rightarrow kl_1$ ,  $\xi \rightarrow \xi/l_1$ , and energies and their variations have been divided by a common prefactor  $\gamma$ .

## 2.3 The cycloid approximation for the no-gravity case

In treating the cycloid approximation, we choose an approach that is essentially variational in nature. Therefore, we need not compute the energy itself but only its variation. The variation of strain energy due to a configurational variation  $\delta\mathbf{x}$  may be written as

$$\delta E_e = \int w(s)\mathbf{n} \delta\mathbf{x} ds. \quad (9)$$

where  $w(s)$  is the energy density at the surface,  $\mathbf{n}$  is the normal vector and  $s$  denotes the arclength along the surface (as we are dealing with a two-dimensional system).

Using Eqs. (2a) and (4), we can calculate an approximation to  $\delta E_e$ , allowing only the parameter  $\rho$  to vary (instead of taking the full variational derivative which would take the result out of the space of cycloidal shapes)

$$\begin{aligned}\delta \mathbf{x} &= \left( \frac{\partial x(\xi)}{\partial \rho} \mathbf{e}_x + \frac{\partial y(\xi)}{\partial \rho} \mathbf{e}_y \right) \delta \rho \\ &= -k^{-1} [\sin(k\xi) \mathbf{e}_x + (\cos(k\xi) + \rho) \mathbf{e}_y] \delta \rho,\end{aligned}\quad (10)$$

and we have the relation

$$\begin{aligned}\mathbf{n} ds &= (-\dot{y}(\xi) \mathbf{e}_x + \dot{x}(\xi) \mathbf{e}_y) d\xi \\ &= [(-\rho \sin(k\xi)) \mathbf{e}_x + (1 - \rho \cos(k\xi)) \mathbf{e}_y] d\xi.\end{aligned}\quad (11)$$

The calculation of the strain energy density can be performed for the general case of a multi-cycloid. Essentially the same calculation has been carried out before by Yu and Suo [18], who used it to model groove-to-crack evolution in ceramics, a context quite different from ours. Since the notations used by the two groups are pretty different and a direct translation would be tedious, we present the important steps of our calculation (done independently and based on [14] rather than [18]) in appendix A. At this point we only need the energy density for the mono-cycloidal surface:

$$w(s) = \frac{1}{2} \frac{(1 - \rho^2)^2}{(1 + \rho^2 - 2\rho \cos(k\xi))^2}. \quad (12)$$

When comparing with the results of [15], one finds the only difference (up to prefactors) in the different sign of the cosine function, which results from their different ansatz of the generating function, corresponding to a simple shift of the argument of the cosine. The integration yields a surprisingly simple result:

$$\frac{\partial E_e}{\partial \rho} = \frac{1}{k} \int w(s) \cos(k\xi) (\rho^2 - 1) d\xi = -\frac{2\pi\rho}{k^2}, \quad (13)$$

where we have taken  $k > 0$  (otherwise the expression on the right-hand side would have to be multiplied by the sign of  $k$ ).

It remains to be noticed that the integration can be done analytically in the mono-cycloid case, yielding

$$E_e = -\frac{\pi\rho^2}{k^2}. \quad (14)$$

The surface energy in our scalings simply is the difference of the arc lengths, and its derivative is calculated straightforwardly:

$$E_s = \int \sqrt{\dot{x}(\xi)^2 + \dot{y}(\xi)^2} d\xi - 1, \quad (15a)$$

$$E_s = \frac{4(1 + \rho)}{k} E\left(\frac{2\sqrt{\rho}}{1 + \rho}\right) - 1, \quad (15b)$$

$$\frac{\partial E_s}{\partial \rho} = \frac{2}{k} \left[ \frac{\rho - 1}{\rho} K\left(\frac{2\sqrt{\rho}}{1 + \rho}\right) + \frac{\rho + 1}{\rho} E\left(\frac{2\sqrt{\rho}}{1 + \rho}\right) \right]. \quad (16)$$

Herein,  $K$  and  $E$  are complete elliptic integrals of the first and second kind, respectively, defined by

$$K(u) = \int_0^{\pi/2} \frac{dx}{\sqrt{1 - u^2 \sin^2 x}}, \quad (|u| < 1), \quad (17a)$$

$$E(u) = \int_0^{\pi/2} dx \sqrt{1 - u^2 \sin^2 x}, \quad (|u| \leq 1). \quad (17b)$$

The result (16) simplifies to  $\partial E_s / \partial \rho = 4/k$  in the fully cusped limit, i.e., for  $\rho = 1$ . For later simplifications we set

$$N(\rho) := \frac{2}{\pi} \left( (\rho - 1) K\left(\frac{2\sqrt{\rho}}{1 + \rho}\right) + (\rho + 1) E\left(\frac{2\sqrt{\rho}}{1 + \rho}\right) \right),$$

leading to

$$\frac{\partial E_s}{\partial \rho} = \frac{N(\rho)\pi}{k\rho}. \quad (18)$$

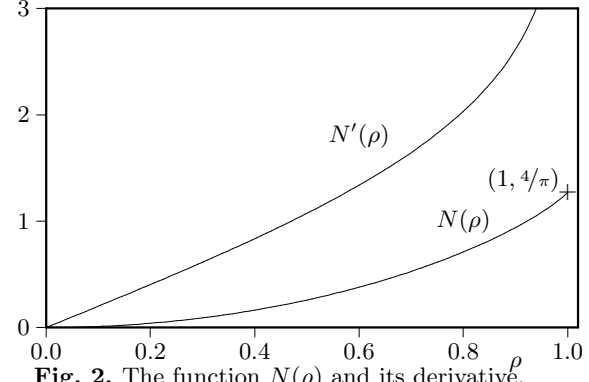


Fig. 2. The function  $N(\rho)$  and its derivative.

In Fig. 2, we plot the function  $N(\rho)$  and its derivative  $dN(\rho)/d\rho = 4\rho K(2\sqrt{\rho}/(1+\rho))/[\pi(1+\rho)]$ . First, we note that  $N(\rho)$  is monotonously increasing from  $N(0) = 0$  to  $N(1) = 4/\pi$ . Second, the derivative diverges logarithmically near  $\rho = 1$ . At  $\rho = 0$ ,  $N(\rho)$  is regular, and the first few terms of its Taylor series are given by

$$N(\rho) = \rho^2 + \frac{1}{8}\rho^4 + \frac{3}{64}\rho^6 + \frac{25}{1024}\rho^8 + \mathcal{O}(\rho^{10}). \quad (19)$$

This expansion will become useful later in the discussion of the type of bifurcation at the instability threshold.

To obtain the energy minimum, we simply have to solve

$$\frac{\partial E_e}{\partial \rho} + \frac{\partial E_s}{\partial \rho} = \frac{2\pi}{k} \left[ -\frac{\rho}{k} + \frac{N(\rho)}{2\rho} \right] = 0. \quad (20)$$

The complete branch is obtained by solving Eq. (20) for  $k$  instead of  $\rho$ , taking into account that  $\rho$  is running from zero to one:

$$k = \frac{2\rho^2}{N(\rho)}. \quad (21)$$

The solution, additionally converted to  $\bar{\alpha}$  via equation (5) for easier comparison, is shown in figure 3. At the termination point of the numerical solution [10], the  $\bar{\alpha}$  value of the mono-cycloid approximation is about 10% smaller.

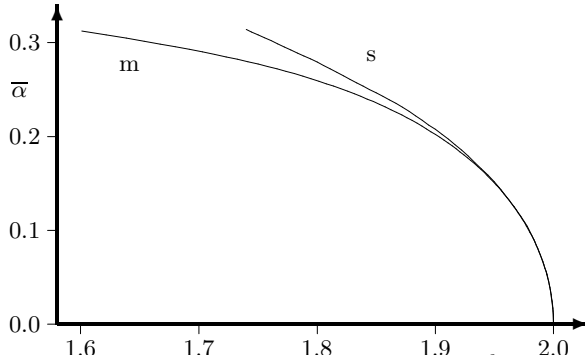


**Fig. 3.** The solution of the mono-cycloid model (m) in comparison with the digitized and scaled solution branch of Spencer and Meiron (s).

From (21), we conclude that the analytical termination point, given by the cusp limit  $\rho=1$ , is located at  $k=\pi/2$ , which is somewhat different from the termination point of Spencer and Meiron [10] at about 1.74 (their scalings imply double wave number and half amplitude with respect to ours, so they gave the termination point at  $k=3.48$ ). We shall see later that the wavenumber of the true cusp is closer to the monocycloid result than to the numeric value. This is due to the fact that a very small change of tip radius in the minimum of the pattern leads to a relatively large change of the wave number. So the Spencer-Meiron result is accurate for the part of the solution branch that it reproduces, but it misses a considerable piece of the branch.

From Eq. (5) we find using  $k_{\text{term}} = \pi/2$

$$\bar{\alpha}_{\text{term}} = \frac{1}{\pi}. \quad (22)$$

An important question is the stability of our solutions. Again, only a simple calculation needs to be performed: Take  $k$  from equation (21), and insert it into the second derivative of the total energy  $E = E_e + E_s$ . This leads to

$$\begin{aligned} \frac{k}{2\pi} \frac{\partial^2 E}{\partial \rho^2} &= -\frac{1}{k} - \frac{N(\rho)}{2\rho^2} + \frac{N'(\rho)}{2\rho} = -\frac{N(\rho)}{\rho^2} + \frac{N'(\rho)}{2\rho} \\ &= \frac{2}{\pi} \left[ \frac{1+\rho}{\rho^2} E \left( \frac{2\sqrt{\rho}}{1+\rho} \right) + \frac{1}{(1+\rho)\rho^2} K \left( \frac{2\sqrt{\rho}}{1+\rho} \right) \right], \quad (23) \end{aligned}$$

which is positive for any  $\rho \in (0, 1)$ . Hence the complete solution branch is stable up to the singularity, a result that agrees with that of Spencer and Meiron [10]. Of course, with our method statements about stability can be made only concerning the restricted set of functions used in the variational ansatz (which depends on just one parameter here).

Beyond  $\rho = 1$ , Eq. (20) still gives us a stationary point of the energy (even a minimum for  $\rho$  not too far above 1), but the corresponding cycloid self-intersects, hence the solution is unphysical. Therefore, the variational ansatz provides a transparent analytic explanation of the fact that the solution branch terminates.

### 3 Including gravity

The next natural step is the incorporation of gravity into the model. Again, the calculation of the corresponding energy contribution is fairly easy, because up to a prefactor it is nothing but the square of the mean square amplitude.

$$E_g = \frac{l_{12}}{2} \int \dot{x}(\xi) y(\xi)^2 d\xi = \frac{\pi l_{12} \rho^2 (2 - \rho^2)}{4 k^3} \quad (24)$$

Consequently, the derivative is

$$\frac{\partial E_g}{\partial \rho} = \frac{\pi l_{12} \rho (1 - \rho^2)}{k^3}, \quad (25)$$

and for the generalized model we replace Eq. (20) by

$$\frac{\partial}{\partial \rho} (E_e + E_s + E_g) = 0. \quad (26)$$

Again it turns out that the solution can be written down exactly if we express  $k$  through  $\rho$ . Now we have two solutions which are both meaningful:

$$k = \frac{\rho^2}{N(\rho)} \left( 1 \pm \sqrt{1 - N(\rho) \frac{1 - \rho^2}{\rho^2} l_{12}} \right) \quad (27)$$

As in the no-gravity case, we construct solution branches by fixing  $l_{12}$  and calculating  $(k, \rho)$  pairs which may then be converted via Eq. (5) into  $(k, \bar{\alpha})$  pairs.

Only the solutions for  $l_{12} \in [0, 1]$  cover the whole range  $\rho = 0 \dots 1$ , while in the region  $l_{12} > 1$ , i.e., below the critical point, the system is linearly stable and hence we find no solutions close to zero. In these cases it is necessary to first calculate the minimum possible value of  $\rho$  by requiring the radicand in Eq. (27) to be zero.

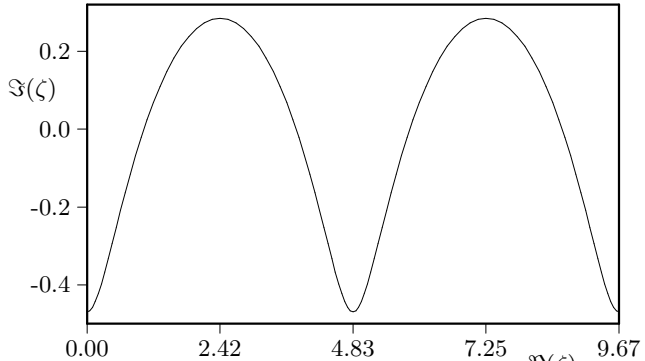
Clearly, the fact that finite-amplitude solutions exist at subcritical values of  $l_{12}$  is already indicative of the subcriticality of the bifurcation at the threshold, a result first obtained by Nozières [19]. Let us discuss the vicinity of the critical point in some more detail. The neutral mode emerging at that point has of course  $\rho = 0$ . So we should expand the energy or its derivative for small  $\rho$  to obtain the solution behavior at the bifurcation. Using Eq. (19), we find for the derivative of the total energy:

$$\begin{aligned} \frac{k}{2\pi} \frac{\partial E}{\partial \rho} &= \left( -\frac{1}{k} + \frac{1}{2} + \frac{l_{12}}{2k^2} \right) \rho \\ &+ \left( \frac{1}{16} - \frac{l_{12}}{2k^2} \right) \rho^3 + \frac{3}{128} \rho^5 + \frac{25}{2048} \rho^7 + \dots \quad (28) \end{aligned}$$

At the bifurcation point, the linear term vanishes, because  $k = 1$  and  $l_{12} = 1$ . The third-order term is  $-7/16 \rho^3$ , i.e., it is negative, whereas higher-order terms are positive. This is to be contrasted with the Nozières calculation and its extension by ourselves in [17], showing that all the calculable coefficients of an amplitude expansion in terms of Fourier modes are negative. From this phenomenon we concluded that there is no restabilization at finite amplitude. At first sight, the situation seems to be different here, due to the

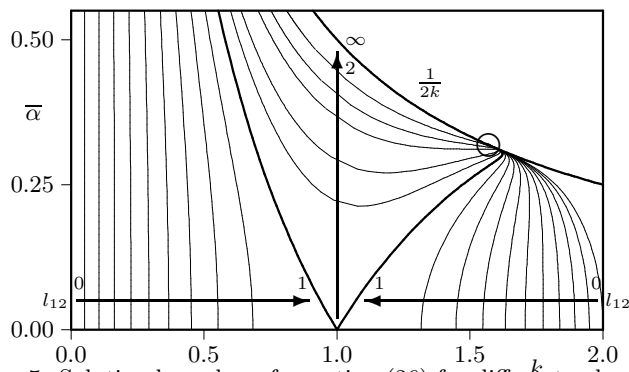
positivity of higher-order coefficients. But in fact, it is not, because the maximum meaningful amplitude is  $\rho = 1$ , and it is easy to see that for this value the third-order coefficient remains dominant. As  $\rho \rightarrow 1$ , the energy derivative tends to the negative value  $4 - 2\pi$ . In a sense, this consideration shows a little more than the calculation in terms of Fourier modes: restabilization of the structure would be possible at  $\rho > 1$ , but this is an unphysical situation.

Figure 4 shows an example for the profile of a steady state-solution taken from the critical branch ( $l_{12} = 1$ ). The solution shows the typical behavior predicted by Nozières, i.e., flat cell tips and sharp grooves. It is however unstable, as shall be seen from the discussion below.



**Fig. 4.** Two periods of a sample solution at  $k = 1.5$ ,  $\Re(\zeta) = 0.25$  (which corresponds to  $\rho \approx 0.49$ ).

A number of solution branches for different values of  $l_{12}$  is shown in Fig. 5. In this plot, we first of all see how the range of unstable wave numbers, starting with the interval  $(0, 2)$  becomes narrower with increasing  $l_{12}$ , i.e., higher gravity or lower prestress. At  $l_{12} = 1$ , only a single  $k$  value has a non-negative growth rate; this is the critical case.



**Fig. 5.** Solution branches of equation (26) for different  $k$  values of  $l_{12}$ . The rightmost curve, beginning at  $(k, \bar{\alpha}) = (2.0, 0.0)$ , is the no-gravity solution shown in Fig. 3. Arrows and small numbers denote  $l_{12}$  values corresponding to the curves. The upper thick line is the limiting curve for large  $l_{12}$ . The common termination point of all branches is marked by a circle. For more details of this region see Fig. 6.

At even higher values of  $l_{12}$ , we are in the subcritical range where it takes some energy to modulate the surface in order to overcome the energy barrier to let the instability emerge. In Fig. 5, we have shown solutions up to  $l_{12} = 2$ . The solution branches converge towards  $\bar{\alpha} = 1/2k$  as  $l_{12}$  is increased, which is the transformation of the cusp limit  $\rho = 1$  (see equation (5)). The common endpoint of all curves  $(\pi/2, 1/\pi)$  is marked with a circle.

Again, as in the no-gravity case we have to check the stability of the solutions by inserting the corresponding solution (27) into the second derivative of the energy. First we note that all branches left of  $k = \pi/2$  in Fig. 5 start off unstably. But there is a range of stability which we discuss with the help of Fig. 6 rather than 5.

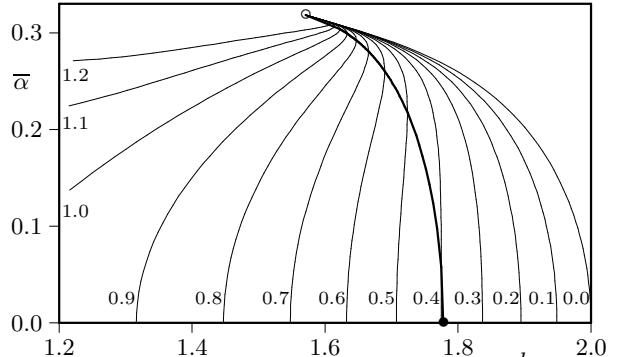


**Fig. 6.** Solution branches of equation (26) in a  $k$ -range. The region bounded by the no-gravity solution and the curve (thick line) from the bullet symbol up to the cusp point contains the stable solutions.

In this figure, we have included the range of stable amplitude solutions. The largest  $l_{12}$  value where *small* solutions still emerge stably (•) is  $l_{12} = 32/81$ , corresponding to  $k = 16/9$ . This should be compared with the result of [17], where the tricritical point is shown to be located at  $k = 13/3 - \sqrt{57}/3 \approx 1.82$ , corresponding to  $l_{12} = 20\sqrt{57}/9 - 148/9 \approx 0.33$ . Because the result from the amplitude equations is exact at infinitesimal amplitudes, the variational ansatz overestimates the range of supercritical bifurcation at lowest order. Of course, such a comparison is a bit unfair towards the variational approach, as we have only a single parameter available there, whereas the lowest-order nonlinear mode expansion contains already two amplitudes. As soon as we take the multi-cycloid ansatz, discussed below, to second order, we obtain the exact position of the tricritical point within this ansatz as well. This is simply due to the fact that the  $n$ -th summand in the multi-cycloid expression (Eq. 29) does not contain Fourier modes lower than  $n$ , hence all contributions of order 2 must be present for  $N = 2$  (but some are already present for  $N = 1$ ).

An interesting fact is the bending of all solution branches into a stable region before running into the cusp, a feature not obtained within the amplitude equation approach. Actually, the stability changes at the points where the slope turns negative (passing from  $+\infty$  to  $-\infty$ ). This can be interpreted as a hint for the existence of stable so-

lution branches at high gravity. These stable solutions do not, at least in the mono-cycloid approximation, emerge at the upper marginal wave number  $1 + \sqrt{1 - l_{12}}$  predicted by the linear stability analysis but instead in the (upper) vicinity of  $k = \pi/2$  at nonzero amplitude. Whether this is really true, will be checked in the following chapters by the implementation of the multi-cycloid ansatz.

## 4 The multi-cycloid approximation

In seeking a generalization of the cycloid ansatz, we were guided by two principles. First, the generalization should reduce to the cycloid, when all but one of the parameters became small. Second, it should correspond to a boundary curve that allows us the analytic solution of the elastic problem by conformal mapping.

Given these conditions, the multi-cycloid model is a natural generalization of the cycloid one (and of a two-cycloid ansatz already considered in [14]):

$$\zeta(\xi) = \xi - i \sum_{n=1}^N \frac{\rho_n}{nk} e^{-ink\xi}. \quad (29)$$

Herein,  $N$  is the number of "cycloid modes" taken into account. The denominator  $n$  in this equation which could also have been included into the definition of the  $\rho_n$  has been explicitly written in order to be able to express the generalized cusp condition in a compact way. Real and imaginary parts read:

$$x(\xi) = \xi - \sum_{n=1}^N \frac{\rho_n}{nk} \sin(nk\xi), \quad (30a)$$

$$y(\xi) = - \sum_{n=1}^N \frac{\rho_n}{nk} \cos(nk\xi). \quad (30b)$$

Again we shift the interface by its mean value to set the average interface position equal to zero:

$$m = \frac{k}{2\pi} \int \dot{x}(\xi) y(\xi) d\xi = \frac{1}{2k} \sum_{n=1}^N \frac{\rho_n^2}{n}, \quad (31)$$

and we have to correct Eq. (30b) as follows:

$$y(\xi) = - \sum_{n=1}^N \frac{\rho_n}{nk} \left( \cos(nk\xi) + \frac{\rho_n}{2} \right). \quad (32)$$

Moreover, we will need the mean square amplitude again. The result is

$$\bar{\alpha} = \left| \frac{1}{k} \sqrt{ \sum_{n=1}^N \left[ \frac{\rho_n^2}{2n^2} \left[ 1 - \frac{n}{2} \sum_{j=1}^N \frac{\rho_j^2}{j} \right] - \sum_{j=1}^{N-n} \frac{\rho_n \rho_j \rho_{n+j}}{j(n+j)} \right] } \right|. \quad (33)$$

We assume the sequence of the  $\rho_n$  to decrease sufficiently fast so the sum of the absolute values of the  $\rho_n$  does not

exceed one, a condition that is sufficient to avoid self-crossings of the curve given by (29). Then cusps, if they exist, can appear only at

$$\xi_{\text{cusp}} k = 2\pi n, \quad n \in \mathbb{N}. \quad (34)$$

(They are characterized by  $\zeta'(\xi) = 0$ .) The radius of curvature is given as [20]

$$r = \left| \frac{(\dot{x}(\xi)^2 + \dot{y}(\xi)^2)^{\frac{3}{2}}}{\left| \begin{array}{l} \dot{x}(\xi) \dot{y}(\xi) \\ \ddot{x}(\xi) \dot{y}(\xi) \end{array} \right|} \right|, \quad (35)$$

and it takes its minimum value at  $\xi = \xi_{\text{cusp}}$ . Therefore,

$$r_{\xi=0} = \left| \frac{\left( -1 + \sum_{n=1}^N \rho_n \right)^2}{k \sum_{n=1}^N n \rho_n} \right|, \quad (36)$$

and the cusp condition reads

$$\sum_{n=1}^N \rho_n = 1. \quad (37)$$

Now the derivatives of the relevant energies have to be calculated. Note that the integration for the energies themselves may not be carried out analytically for general multi-cycloids. But the question of stability of the solution can be answered, because first and second derivative can be given explicitly.

The crucial point is the calculation of the elastic energy density  $w(s)$  at the surface, which is done in appendix A. Supposing  $w(s)$  is given (see Eq. (59)), we have to modify Eqs. (10) and (11) as follows (we write  $C_n$  and  $S_n$  instead of  $\cos(nk\xi)$  and  $\sin(nk\xi)$ ):

$$\begin{aligned} \delta \mathbf{x} &= \sum_{n=1}^N \left( \frac{\partial x(\xi)}{\partial \rho_n} \mathbf{e}_x + \frac{\partial y(\xi)}{\partial \rho_n} \mathbf{e}_y \right) \delta \rho_n \\ &= - \frac{1}{nk} \sum_{n=1}^N [S_n \mathbf{e}_x + (C_n + \rho_n) \mathbf{e}_y] \delta \rho_n, \end{aligned} \quad (38)$$

$$\mathbf{n} ds = (-\dot{y}(\xi) \mathbf{e}_x + \dot{x}(\xi) \mathbf{e}_y) d\xi \quad (39)$$

Consequently, we get according to Eq. (9)

$$\frac{\partial E_e}{\partial \rho_n} = \frac{1}{nk} \int w(s) [S_n \dot{y}(\xi) - (C_n + \rho_n) \dot{x}(\xi)] d\xi. \quad (40)$$

The other terms are simpler again. Gravitational energy is  $l_{12}/2$  times the square of the mean square amplitude (33)

$$E_g = \frac{l_{12}}{2} \bar{\alpha}^2, \quad (41)$$

if we divide the integral by the wavelength, as we will do in all energy expressions from now on, i.e., rather than

integrals over a periodicity unit we consider averages. We obtain

$$\frac{\partial E_g}{\partial \rho_n} = \frac{l_{12}}{2k^2} \left[ \frac{\rho_n}{n} \left( \frac{1}{n} - \sum_{j=1}^N \frac{\rho_j^2}{j} \right) - \sum_{j=1, j \neq n}^N \frac{\rho_j \rho_{|n-j|}}{n|n-j|} \right], \quad (42)$$

and the surface tension is again represented by the difference of the arc lengths (compare Eq. (15a)), hence its derivative reads after some simplification

$$\frac{\partial E_s}{\partial \rho_n} = \int d\xi \left[ \frac{\rho_n - C_n + \sum_{l=1}^{n-1} C_l \rho_{n-l} + \sum_{l=1}^{N-n} C_l \rho_{n+l}}{\sqrt{1 + f(\bar{\rho}, \xi)}} \right],$$

$$f(\bar{\rho}, \xi) = \sum_{l=1}^N \rho_l (\rho_l - 2C_l) + 2 \sum_{l=1}^{N-1} C_l \sum_{j=1}^{N-l} \rho_j \rho_{j+l} \quad (43)$$

This integral can only be solved analytically for the case  $N = 1$ ; the analytical result has been used in the monocycloid model.

Equipped with the terms (40), (42) and (43) we can now numerically solve the system

$$\frac{\partial}{\partial \rho_n} (E_e + E_s + E_g) = 0, \quad n = 1 \dots N, \quad (44)$$

for the set  $\{\rho_1 \dots \rho_N\}$ , given a certain prescribed  $k$  value. Some technical details of the solution method are described in appendix B.

We have carried out the calculations for a range of  $N$  up to 50. Figure 7 shows how fast the effective amplitude branches converge to the numerical result from [10].

A means to assess the closeness of a solution branch to its cusp termination is to determine the radius of curvature in the minimum of the grooves which will approach zero near the cusp. Here we note that the  $N = 3$  approximation is insufficient for a description of the tip radius (Fig. 8), in contrast with the effective amplitude (Fig. 7), which is already well approximated by three modes for most of the branch. (We have omitted  $N = 2$  here because it is much worse.)

As can be seen, the solutions agree with the Spencer solution in the range they cover. Yet, the extension to the range of lower wavenumbers is rather sensitive to the number of included modes. A prolongation of the curves in Fig. 8 suggests a termination point slightly left of  $k = 1.55$ , which is less than  $\pi/2$  as proposed by the monocycloid model. As with increasing  $N$  the termination point moves to slightly higher values of  $k$ , it is tempting to speculate that the exact termination point is at  $k = \pi/2$  indeed. In any case, our method allows to reach radii of curvature that are three orders of magnitude smaller than the minimum value found by Spencer and Meiron, and it does so apparently with less numerical effort.

The incorporation of gravity has been carried out up to  $l_{12} = 1$ . Figure 9 gives the solution branches, unstable curves left of  $k = 1$  are not shown. We note that the

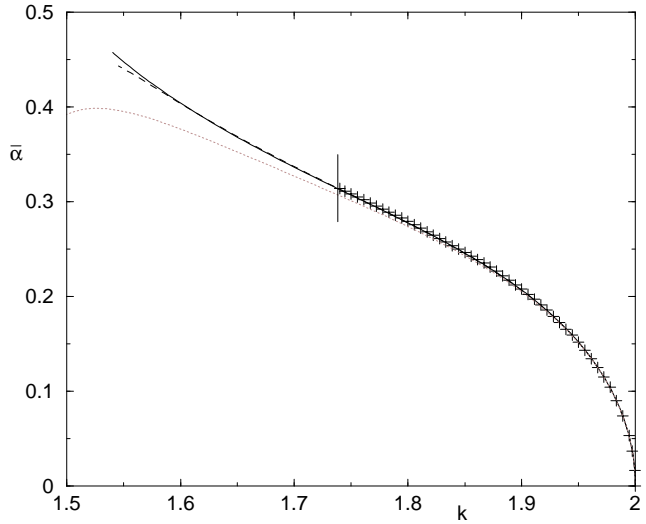


**Fig. 7.** Comparison of the  $N = 2, 3$  and 10 multi-cycloid models in the no-gravity case. The dotted line is the  $N = 2$  approximation, which is insufficient for our purpose: it does not reach the cusp at all but turns into a bag-like morphology instead (i.e., it develops overhangs). The dashed line is  $N = 3$ , being already in good agreement with [10], and the solid line is the  $N = 10$  example. All solutions with  $N \geq 4$  look the same. Curves are terminating slightly before the cusp emerges, which will be further clarified in fig.8. The crosses represent the numerical solution from [10].

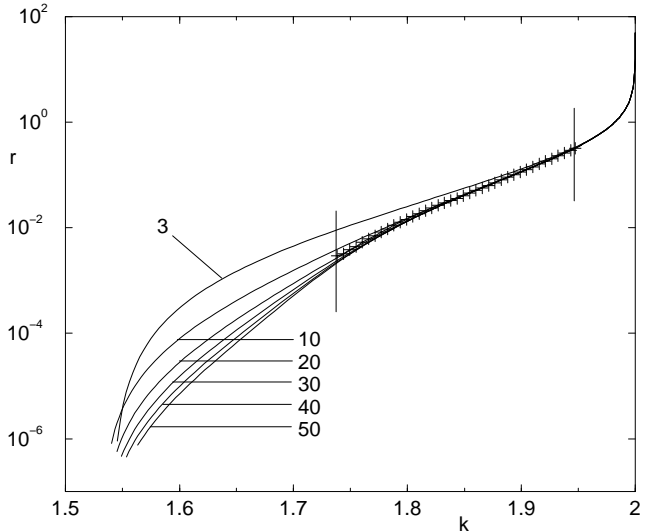


**Fig. 8.** Radii of curvature for  $N$  up to 50, explanations see text. Again, the crosses show the digitized and scaled radii of curvature of the Spencer solution.

common cusp point, an important feature of Fig. 6, disappears. As in Fig. 7, the curves terminate before the cusp is actually reached.

Stability of the solutions is checked via computation of the determinant of the matrix  $\partial^2 E / \partial \rho_n \partial \rho_m$  and its principal minors. If all of these are positive, the matrix is positive definite, the energy has a minimum and the solution is stable. As it turns out, the determinant itself gets

positive only after its minors, so it would in our case be sufficient to check the sign of the determinant alone. The range of stable solutions is displayed as the grayed area in Fig. 9. We conclude that the stability behavior is qualitatively correctly described by the mono-cycloid model already. However, stability sets in at smaller amplitudes for  $k$  values below 1.7. Hence, the multi-cycloid modes act stabilizing at larger amplitudes and destabilizing near the tricritical point, which is shifted to larger  $k$  by inclusion of the second mode.

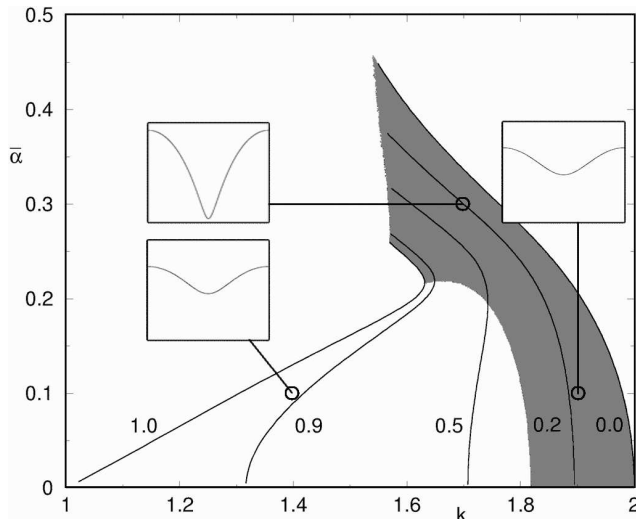


**Fig. 9.** Solution branches based on a  $N = 30$  multi-cycloid approximation. Numbers denote the value of  $l_{12}$ . The shaded area indicates the stable part of the solution manifold. Small sub-figures represent example morphologies.

The subfigures of 9 show that up to the different distances to the cusp, which make the curves more or less "sharp", there is no indication from the shape itself whether it is stable or not.

## 5 Summary

To conclude, we have presented a variational approach to the calculation of steady states for the Grinfeld instability. Taking into account a single mode we already obtain a very nice qualitative description of the system behavior including the approach to a cusped state. The wavenumber for the cusp appearance is already more accurate with a single mode than in the article of Spencer and Meiron, while the amplitude is pretty far off the true result (by about the same amount as the amplitude obtained by Spencer and Meiron).

Nevertheless, this single-mode approximation has the virtue of great transparency. That a cusp singularity appears is rendered understandable: the system simply draws near a state where further minimization of the elastic energy would require the interface to self-intersect.

A few words may be in order concerning the limits of validity of our approach. The nature of our calculation

is variational, which means that it will overestimate the energy of the system. Moreover, the minima of the variational energy will not lie exactly at the same positions in parameter space as those of the true energy. As we increase the number of modes, we will get closer to the true result, and if our function system were complete, we could be certain of full convergence of the variational results to the correct answer. We have no formal proof of the completeness of the system of multi-cycloids but note that as a function of  $\xi$ , the systems used for the representation of the abscissa and the ordinate of the curve are complete in the spaces of odd and even functions, respectively. Completeness is difficult to prove because of the correlation between the coefficients describing the abscissa and the ordinate. However, we suspect that for all practical purposes of representing curves that resemble a cycloid as closely as do the numerically obtained solutions, our function system can be considered complete.

In the full numerical computation [10], with which we compared our results, the discretization of abscissae is given by a formula akin to (2a) with an equidistant distribution of the parameter  $\xi$  and the interface position is given as a superposition of cosine modes in the same parameter. Hence, numerical convergence relies on the assumption of completeness of a function system derived from Fourier modes by a stretching in the  $x$  coordinate.

As long as the higher modes have small enough amplitudes, the two approaches should give equivalent results. Since we solve the elastic problem essentially analytically and for a continuous interface, not a discrete one, we reach the same accuracy as the numerics with fewer modes.

Note that the cusp singularity is *not* an inherent restriction to the method, as the function system is chosen such that it can represent one (or several) cusps. However, when a cusp appears, quantities such as the elastic energy density diverge there. This means that the numerical solution of the nonlinear system of equations (44) for the variational parameters will run into problems, hence the cusp cannot be reached exactly in this final numerical step.

Even the one-mode approximation suggests the existence of stable large-amplitude steady states in the presence of gravity, as is demonstrated by Fig. 6. Taking into account more modes, we obtain a quantitatively satisfactory description of the numerical Spencer-Meiron branch, conveying some confidence that the new branches with gravity are equally well described by this approach. The stability domain suggested by the one-mode picture is roughly confirmed in the three-mode representation (see Fig. 9). As gravity is increased, there are no small-amplitude stable solutions anymore. At first sight, this might seem counterintuitive: why should gravity, a stabilizing effect, destroy the stability of small-amplitude solutions? The answer is that gravity renders the zero-amplitude, i.e. planar, solution more stable and hence larger amplitudes are needed for true structures to become stable.

Hence, we conclude that in *confined* systems under gravity or a similar body force (it has been shown that in directional solidification a temperature gradient acts

just as a strong effective gravity field [21, 7]) stable steady states may exist at large amplitude and be absent at small ones.

Below the instability threshold, i.e., for parameters where the planar interface is stable, the system may be forced into a large amplitude state by a sufficiently strong perturbation. This clearly calls for numerical simulations and experimental attempts at creating these states.

In *extended* systems, the absence of stable steady-state solutions at large wavelength as well as the numerical evidence from time-dependent simulations [10, 14] suggest that the cusp singularity is indeed reached in finite time. This is of course a statement within linear elasticity theory. It means that stresses would increase beyond all limits in the minimum of a groove, if linear elasticity held all the time. If linear elasticity were valid up to the fracture threshold, one might conclude from this result that the Grinfeld instability would inevitably lead to fracture in such a situation. However, the answer to this question is beyond the scope of this paper, as it is obvious that at sufficiently large stresses plasticity must be taken into account. Phase-field simulations containing an inherent yield stress in the model [14] suggest that indeed cracking is a likely scenario in sufficiently extended systems.

This work was supported by the *Deutsche Forschungsgemeinschaft* under Grant No. Ka 672/4-2 and FOR 301/2-1, which is gratefully acknowledged. In addition, we acknowledge travel grants by PROCOPE, Grant No. 9619897 (DAAD, Germany) and 97176 (APAPE, France), enabling a closer collaboration between the two groups involved in this work.

## A Calculation of the strain energy density along a multi-cycloid surface

Instead of calculating the strain energy density inside the bulk as in [17], we will only describe here how to calculate this energy density  $w(s)$  at the surface. We carry out the calculation for general  $N$ -cycloids.

In general, the elastic energy density of a solid submitted to plane strain can be written in terms of the two-dimensional stress tensor as

$$w = \frac{1+\nu}{2E} (\sigma_{ij}\sigma_{ij} - \nu\sigma_{kk}^2) , \quad (45)$$

where summation over repeated subscripts is implied. At the interface,  $\sigma_{ij}$  is diagonal with elements  $\sigma_{tt}$  and  $\sigma_{nn}$ . Since  $\sigma_{tt} = \text{Tr } \sigma - \sigma_{nn}$  and because in our normalization  $\sigma_{nn} = 0$ , the elastic energy density can be expressed by the trace of the stress tensor alone, which allows us to deal with a single scalar. Thus the strain energy density takes the form

$$w(x, y) = \frac{1}{2} (\text{Tr } \sigma)^2 , \quad (46)$$

where  $\text{Tr } \sigma$  is in our non-dimensional scalings equal to  $1 + \sigma_{xx} + \sigma_{yy}$ .

The idea is to employ a mapping of the half-plane bounded from above by our multi-cycloid onto the area

below the real axis using the analytic function

$$z = \omega(\zeta) = \zeta - i \sum_{n=1}^N \frac{\rho_n}{nk} e^{-ink\zeta} , \quad (47)$$

where  $\zeta = \xi + i\eta$ . This defines a mapping of the domain  $\Im(z) \leq \zeta$  to the lower  $\zeta$  half plane, as can be seen easily by restricting to  $\zeta = \xi$  which shows that the interface is mapped to the real axis. In order to solve the elastic problem we have to satisfy [14]

$$\phi_0(\xi) + [\omega(\xi) - \bar{\omega}(\xi)] \frac{\overline{\phi'_0}(\xi)}{\overline{\omega'}(\xi)} + \overline{\psi'_0}(\xi) = \frac{\bar{\omega}(\xi) - \omega(\xi)}{2} , \quad (48)$$

where  $\phi_0$  and  $\psi_0$  are modified Goursat functions. These functions must be analytic functions of  $\zeta$  for  $\eta \rightarrow -\infty$ , so it has to be established that  $\psi'_0(\xi)$  contains no exponentials increasing for  $\eta \rightarrow -\infty$  when  $\xi$  is replaced by  $\xi + i\eta$ . Since  $\overline{\psi'_0}(\xi)$  is the complex conjugate of a function that is analytic in the *lower* half plane, it must be analytic in the *upper* half plane, which means that terms of the form  $\exp(in\xi)$  are allowed whereas  $\exp(-in\xi)$  are not (for details see [14]). For brevity, we will designate the forbidden terms as “negative exponentials”. Technically, we make an ansatz for  $\phi_0(\xi)$ :

$$\phi_0(\xi) = \frac{i}{k} \sum_{n=1}^N \alpha_n e^{-ink\xi} , \quad (49)$$

where we may assume  $\alpha_n$  to be real (which will be justified later). Now let us simplify Eq. (48). We have

$$[\omega(\xi) - \bar{\omega}(\xi)] = 2i\Im(\omega(\xi)) = -\frac{2i}{k} \sum_{n=1}^N \frac{\rho_n}{n} C_n \quad (50)$$

and hence

$$\overline{\psi'_0}(\xi) = \frac{1}{k} \sum_{n=1}^N \frac{\rho_n}{n} C_n \left( 1 + 2 \frac{\overline{\phi'_0}(\xi)}{\overline{\omega'}(\xi)} \right) - \phi_0(\xi) . \quad (51)$$

Via the choice of  $\alpha_n$  we have to establish that the right hand side of Eq. (51) contains no negative exponentials. Let us further simplify the representation. We have

$$\overline{\phi'_0}(\xi) = \sum_{n=1}^N n\alpha_n e^{ink\xi} , \quad (52a)$$

$$\overline{\omega'}(\xi) = 1 - \sum_{n=1}^N \rho_n e^{ink\xi} . \quad (52b)$$

For the division, we use the common expression for the quotient of two series ([22], p. 28): Let

$$\begin{aligned} s_1 &= 1 + a_1 x + a_2 x^2 + a_3 x^3 + \dots , \\ s_2 &= 1 + b_1 x + b_2 x^2 + b_3 x^3 + \dots , \\ s_3 &= 1 + c_1 x + c_2 x^2 + c_3 x^3 + \dots , \\ s_4 &= 1 + d_1 x + d_2 x^2 + d_3 x^3 + \dots , \\ s_5 &= 1 + \epsilon_1 x + \epsilon_2 x^2 + \epsilon_3 x^3 + \dots , \end{aligned}$$

with

$$s_1 = 1 + \overline{\phi'_0}(\xi), \quad s_2 = \overline{\omega'}(\xi),$$

that is

$$a_n = n\alpha_n, \quad b_n = -\rho_n, \quad x = e^{ik\xi}.$$

We then need to calculate

$$\begin{aligned} s_3 &= \frac{s_1}{s_2}, \\ s_4 &= s_2^{-1}, \\ s_5 &= s_3 - s_4 = \frac{\overline{\phi'_0}}{\overline{\omega'}}. \end{aligned}$$

The coefficients  $c_n$  and  $d_n$  are given by the recursion

$$\begin{aligned} c_1 &= a_1 - b_1, \\ c_n &= a_n - \left[ b_n + \sum_{j=1}^{n-1} b_j c_{n-j} \right], \\ d_1 &= -b_1, \\ d_n &= - \left[ b_n + \sum_{j=1}^{n-1} b_j d_{n-j} \right]. \end{aligned}$$

This leads to

$$\begin{aligned} \epsilon_1 &= a_1, \\ \epsilon_n &= a_n - \sum_{j=1}^{n-1} b_j \epsilon_{n-j}. \end{aligned} \tag{53}$$

We then have, after introducing  $\epsilon_0 = 1/2$ ,

$$1 + 2 \frac{\overline{\phi'_0}(\xi)}{\overline{\omega'}(\xi)} = 1 + 2s_5 = 2 \sum_{n=0}^{\infty} \epsilon_n x^n. \tag{54}$$

Therefore,

$$\begin{aligned} \epsilon_0 &= \frac{1}{2}, \quad \epsilon_1 = \alpha_1, \\ \epsilon_n &= n\alpha_n + \sum_{j=1}^{n-1} \rho_j \epsilon_{n-j}, \quad n = 2 \dots N. \end{aligned} \tag{55}$$

Negative exponentials on the right-hand side of (51) can only result from the negative exponentials in

$$C_n = \frac{1}{2} (e^{ink\xi} + e^{-ink\xi}).$$

We cut out the relevant parts from Eq. (51), consisting of negative exponentials and require them to become zero, to compute the coefficients determining  $\phi_0$  in terms of the  $\rho_n$

$$\left( \sum_{m=1}^N \frac{\rho_m}{m} e^{-imk\xi} \right) \left( \sum_{j=0}^{N-1} \epsilon_j e^{ijk\xi} \right) = \sum_{n=1}^N \alpha_n e^{-ink\xi}, \tag{56}$$

with  $\epsilon_0 = 1/2$  and the prefactor  $ik^{-1}$  dropped. Now we sort the terms in this equation by exponentials which finally gives us the system

$$\alpha_n = \sum_{j=0}^{N-n} \epsilon_j \frac{\rho_{n+j}}{n+j}, \quad n = 1 \dots N. \tag{57}$$

Note that the  $\epsilon_j$  contain the  $\alpha_i$  as well, so the equations are not a simple recursive scheme but a linear system of equations for the  $\alpha_n$ . Now we get back to  $\text{Tr } \sigma$ , which can be written as

$$\text{Tr } \sigma = 1 + 4 \frac{\dot{x}(\xi) \Re(\phi'(\xi)) + \dot{y}(\xi) \Im(\phi'(\xi))}{\dot{x}(\xi)^2 + \dot{y}(\xi)^2}. \tag{58}$$

The denominator has already been written down during the calculation of the arc length. The numerator can be simplified in a similar manner. After all simplifications have been performed, we finally get

$$\begin{aligned} w(s) &= \frac{1}{2} \left( 1 + 4 \frac{w_1(s)}{1 + w_2(s)} \right)^2 \\ w_1(s) &= \sum_{n=1}^N n\alpha_n (C_n - \rho_n) \\ &\quad - \sum_{n=1}^{N-1} C_n \sum_{j=1}^{N-n} (\rho_j \alpha_{j+n} (j+n) + \rho_{j+n} \alpha_j j) \\ w_2(s) &= \sum_{n=1}^N \rho_n (\rho_n - 2C_n) + 2 \sum_{n=1}^{N-1} C_n \sum_{j=1}^{N-n} \rho_j \rho_{j+n}. \end{aligned} \tag{59}$$

## B Details of the numerical solution of Eq. (44)

Let us first repeat the system of partial differential equations (44).

$$\frac{\partial}{\partial \rho_j} [E_e + E_s + E_g] = 0, \quad j = 1 \dots N. \tag{60}$$

Herein, the energy changes entering the equation are integrals over certain rational terms containing trigonometric functions and the vector of amplitudes  $\underline{\rho} = (\rho_1 \dots \rho_N)$  as well as the wave number  $k$  and the gravity parameter  $l_{12}$ .

We first reformulate the problem (60) by considering the fact that  $k$  is contained in the energy terms as a prefactor only (compare Eqs. (40), (42) and (43))<sup>2</sup>. Then we get a simplified problem with modified  $E$  terms:

$$\frac{\partial}{\partial \rho_j} \left[ \frac{1}{k} \tilde{E}_e(\underline{\rho}) + \tilde{E}_s(\underline{\rho}) + \frac{1}{k^2} \tilde{E}_g(\underline{\rho}) \right] = 0. \tag{61}$$

The question is now to specify which subset of the solution manifold is required. We concentrate on fixed physical

<sup>2</sup> De facto we have also transformed the integration variable  $\xi \rightarrow X = k\xi$ , changing the integration interval to  $[0, \pi]$ .

system parameters, i.e., constant  $l_{12}$  in order to produce the lines shown in figure 9.

Next a suitable numerical method has to be chosen. Solutions are known to satisfy  $\underline{\rho} \approx 0$  for  $\bar{\alpha} \approx 0$ , and solutions starting a branch are given by linear stability analysis:  $k_{\text{start}} = 1 + \sqrt{1 - l_{12}}$ ;  $\rho_{j,\text{start}} = 0$ ,  $j = 1 \dots N$ .

As solutions along a branch are expected to change continuously, we can implement a Newton Raphson algorithm and move along the selected branch by varying a parameter. Yet, already in the monocycloid model we find that some of the curves are multi-valued with respect to  $k$ . This renders it unfavourable to use  $k$  as a fixed parameter in that scheme and to solve for  $\rho_1$ , because the exact turning points are unknowns.

It turns out that for all branches situated between  $k = 1$  and  $k = 2$ , and with  $l_{12} \in [0, 1]$ , the curves behave monotonously as a function of  $\rho_1$  up to the cusp. These are the cases exhibited in figure 9. Therefore, in order to solve the system of equations (61) for  $j = 1 \dots N$ , we keep  $\rho_1$  fixed instead of  $k$  and take  $\{k, \rho_2 \dots \rho_N\}$  as our set of variables to be determined by the iteration. This results in a modified Jacobian containing terms  $\{\partial^2 E / \partial \rho_n \partial k, \partial^2 E / \partial \rho_n \partial \rho_m\}$  ( $m = 2 \dots N, n = 1 \dots N$ ).

As initial guess for the first non-zero solution of a branch, we choose the upper marginal wavenumber from linear theory for  $k$ , a small value of  $\rho_1$  and set all other  $\rho_i$  equal to zero. After having found the first solution, we move along the solution branch towards larger  $\rho_1$  values in steps of typically  $\Delta \rho_1 = 0.001$ . Consecutive data sets are estimated by forward differences using up to six solution points and then iterated until the 2-norm of the vector of the changes remains below a threshold of typically  $10^{-10}$ .

It should be emphasized that the derivatives of Eqs. (40), (42) and (43) can be given analytically (they are omitted here because they are rather lengthy expressions), and so the Newton Raphson algorithm can be programmed with an (up to quadrature) exact Jacobi matrix. This makes the code converge extremely fast.

A more thorough investigation of the solution manifold with respect to small wavenumbers and  $l_{12} > 1$  goes beyond the scope of this paper because monotony considerations do not apply in this range and multi-valuedness of the manifold can appear which is connected to coarsened solutions. These considerations will be presented in a separate work.

## References

1. M.A. Grinfeld. *Dokl. Akad. Nauk SSSR*, 290:1358, 1986 [Instability of the Separation Boundary between a Non-Hydrostatically Stressed Elastic Body and a Melt. *Sov. Phys. Dokl.*, 31:831, 1986].
2. M.A. Grinfeld. The Stress Driven Instability in Elastic Crystals: Mathematical Models and Physical Manifestations. *J. Nonlinear Sci.*, 3:35, 1993.
3. M. Grinfeld, Two-dimensional islanding atop stressed solid helium and epitaxial films. *Physical Review B*, 49:8310, 1994.
4. P. Berger, P. Kohlert, K. Kassner, C. Misbah. Pattern Selection in Biaxially Stressed Solids. *Physical Review Letters*, 90:176103, 2003.
5. R.J. Asaro and W.A. Tiller. Interface Morphology Development during Stress Corrosion Cracking: Part I. Via Surface Diffusion. *Metall. Trans. A*, 3:1789, 1972.
6. R.H. Torii and S. Balibar. Helium crystals under stress: the Grinfeld instability. *J. Low Temp. Phys.*, 89:391, 1992.
7. I. Cantat, K. Kassner, C. Misbah, and H. Müller-Krumbhaar. Directional solidification under stress. *Phys. Rev. E*, 58:6027, 1998.
8. W.H. Yang and D.J. Srolovitz. Cracklike surface instabilities in stressed solids. *Phys. Rev. Lett.*, 71:1593, 1993.
9. K. Kassner and C. Misbah. Non-linear evolution of a uniaxially stressed solid: A route to fracture? *Europhys. Lett.*, 28(4):245, 1994.
10. B.J. Spencer and D.I. Meiron. Nonlinear evolution of the stress-driven morphological instability in a two-dimensional semi-infinite solid. *Acta metall. mater.*, 42(11):3629, 1994.
11. J. Kappey. Directional solidification under stress. PhD thesis, Otto-von-Guericke University, Magdeburg, 2000.
12. J. Müller. Study of Stress-Induced Morphological Instabilities PhD thesis, McGill University, Montréal, 1998.
13. J. Müller and M. Grant. Model of Surface Instabilities Induced by Stress, *Phys. Rev. Lett.*, 82:1736, 1999.
14. K. Kassner, C. Misbah, J. Müller, J. Kappey, and P. Kohlert. Phase field under stress. *Phys. Rev. E*, 63:036117, 2001.
15. C.-H. Chiu and H. Gao. Stress singularities along a cycloid rough surface. *International Journal of Solids and Structures*, 30(21):2983–3012, 1993.
16. N. I. Mußchelischwili. *Einige Grundaufgaben zur mathematischen Elastizitätstheorie*. Fachbuchverlag, Leipzig, 1971.
17. P. Kohlert, K. Kassner, and C. Misbah. High-order weakly nonlinear analysis of the Grinfeld instability. 2003, to be published.
18. H.H. Yu and Z. Suo. Delayed fracture of ceramics caused by stress-dependent surface reactions. *Acta Mater.*, 47:77, 1999.
19. P. Nozières. Amplitude expansion for the Grinfeld instability due to uniaxial stress at a solid surface. *J. Phys. I France*, 3:681–686, March 1993.
20. Hans-Jochen Bartsch. *Mathematische Formeln*. Buch- und Zeit-Verlagsgesellschaft mbH, Köln, 15th edition, 1988.
21. I. Durand, K. Kassner, C. Misbah, and H. Müller-Krumbhaar. Strong Coupling between Diffusive and Elastic Instabilities in Directional Solidification. *Phys. Rev. Lett.*, 76:3013, 1996.
22. Milton Abramowitz and Irene A. Stegun, editors. *Pocketbook of Mathematical Functions*. Harri Deutsch, Thun, Frankfurt/Main, 1984. Abridged Edition of "Handbook of Mathematical Functions".